European Journal of Nuclear Medicine and Molecular Imaging (2019) 46:2190–2198
https://doi.org/10.1007/s00259-019-04375-8

ORIGINAL ARTICLE

Influx rate of ^{18}F-fluoroaminosuberic acid reflects cystine/glutamate antiporter expression in tumour xenografts

Kathinka E. Pitman[1,2] · Santosh R. Alluri[3] · Alexander Kristian[4] · Eva-Katrine Aarnes[5] · Heidi Lyng[5] · Patrick J. Riss[3] · Eirik Malinen[1,2]

Received: 27 February 2019 / Accepted: 27 May 2019 / Published online: 1 July 2019

Abstract

Purpose ^{18}F-fluoroaminosuberic acid (^{18}F-FASu) is a recently developed amino acid tracer for positron emission tomography (PET) of oxidative stress that may offer improved tumour assessment over the conventional tracer ^{18}F-fluorodeoxyglucose (^{18}F-FDG). Our aim was to evaluate and relate dynamic ^{18}F-FASu and ^{18}F-FDG uptake with pharmacokinetic modelling to transporter protein expression levels in a panel of diverse tumour xenograft lines.

Methods Four different tumour xenograft lines were implanted in female athymic nude mice: MAS98.12 and HBCx3 (breast), TPMX (osteosarcoma) and A549 (lung). Dynamic PET over 60 min was performed on a small animal unit. The time–activity curves (TACs) for ^{18}F-FASu and ^{18}F-FDG in individual tumours were used to extract early (SUV_E; 2 min p.i.) and late (SUV_L; 55 min p.i.) standardised uptake values. Pharmacokinetic two-tissue compartment models were applied to the TACs to estimate rate constants K_1–k_4 and blood volume fraction v_B. Relative levels of cystine/glutamate antiporter subunit xCT were assessed by western blotting, and expression of GLUT1 and CD31 by immunohistochemistry.

Results ^{18}F-FASu showed higher SUV_E, whilst ^{18}F-FDG exhibited higher SUV_L. Influx rate K_1 for ^{18}F-FASu was significantly correlated with xCT levels ($p = 0.001$) and was significantly higher than K_1 for ^{18}F-FDG ($p < 0.001$). K_1 for ^{18}F-FDG was significantly correlated with GLUT1 levels ($p = 0.002$). v_B estimated from ^{18}F-FASu and ^{18}F-FDG TACs was highly consistent and significantly correlated ($r = 0.85$, $p < 0.001$). Two qualitatively different ^{18}F-FASu uptake profiles were identified: type α with low xCT expression and low K_1 (A549 and HBCx3), and type β with high xCT expression and high K_1 (MAS98.12 and TPMX).

Conclusion The influx rate of ^{18}F-FASu reflects xCT activity in tumour xenografts. Dynamic PET with pharmacokinetic modelling is needed to fully appraise ^{18}F-FASu distribution routes.

Keywords Cancer · Xenograft · Mouse model · System X_C^- · xCT · 18F-fluoroaminosuberic acid · 18F-FDG · Dynamic PET · Pharmacokinetic modelling · Oxidative stress

This article is part of the Topical Collection on Advanced Image Analyses (Radiomics and Artificial Intelligence)

Electronic supplementary material The online version of this article (https://doi.org/10.1007/s00259-019-04375-8) contains supplementary material, which is available to authorized users.

✉ Eirik Malinen
eirik.malinen@fys.uio.no

[1] Department of Physics, University of Oslo, P.O. Box 1048 Blindern, 0316 Oslo, Norway

[2] Department of Medical Physics, Oslo University Hospital, Oslo, Norway

[3] Department of Chemistry, University of Oslo, P.O. Box 1048 Blindern, 0316 Oslo, Norway

[4] Department of Tumour Biology, Oslo University Hospital, Oslo, Norway

[5] Department of Radiation Biology, Oslo University Hospital, Oslo, Norway

Introduction

Positron emission tomography (PET) is an important tool for imaging of cancer, providing a non-invasive means for diagnosis, staging, monitoring of treatment and prediction of treatment response, as well as detection of residual or recurrent disease. Imaging of glucose metabolism by ^{18}F-Fluorodeoxyglucose (^{18}F-FDG) PET is utilised for a large range of cancer types, including lung [1], osteosarcoma [2] and breast cancers [3]. However, reprogrammed glucose metabolism is only one of the hallmarks of cancer aggressiveness and response to therapy [4]. ^{18}F-FDG is not always useful, e.g. for tumours close to organs with naturally high background [4], for tumours with low glycolytic activity [5], or for differentiating inflammatory lesions [6]. A range of tracers exploiting other aspects of cellular metabolism have been introduced, including tracers targeting oxidative stress [7–10]. Oxidative stress is implicated in several features of tumourigenesis, including mutation and initiation, cell proliferation, resistance to apoptosis, angiogenesis, tissue invasion and metastasis [11]. Moreover, adaptation to oxidative stress is instrumental in the development of resistance to chemo- and radiotherapy [12, 13]. X_C^- is a cystine/glutamate antiporter upregulated in response to oxidative stress, consisting of two subunits, of which the light-chain xCT confers specificity [14]. Increased expression of xCT in response to oxidative stress facilitates increased import of cystine, which is intracellularly reduced to cysteine, and may thereafter participate in either of two major independent processes: (i) incorporation into glutathione (GSH), the most important endogenous antioxidant for intracellular reduction, or (ii) export for direct extracellular reduction via the cystine/cysteine redox cycle [15].

Conventional static PET, with quantification in terms of the standardised uptake value (SUV) at typically 60 min post-injection (p.i.), provides a useful but limited picture of how tracer is utilised by tumours. Conversely, dynamic PET with pharmacokinetic compartment modelling may be used to decompose time–activity patterns into estimates of tumour perfusion, vascular permeability, specific binding, and passively accumulated and actively metabolised tracer [16]. This provides insight into temporal distribution in tissue and affords time-invariant measures which may be more directly related to biological data.

Webster et al. recently developed ^{18}F-fluoroaminosuberic acid (^{18}F-FASu), a cystine/glutamate analogue PET tracer, which has shown promising results in ovarian carcinoma and mouse lymphoma models, with improved uptake characteristics over ^{18}F-FDG [9]. Further work by Yang et al. demonstrated its potential utility in diagnosis and stratification of breast cancers, with elevated uptake in a highly xCT-expressing triple-negative breast cancer model [10]. However, it is not clear whether ^{18}F-FASu is superior to ^{18}F-FDG in a broader, unbiased selection of cancer types. In the current work, we have selected two breast cancers of different phenotype: a highly aggressive triple-negative breast cancer with high glucose [17] and choline [18] metabolism, and a more slow-growing tumour line of ER+/PR+ subtype. As the lung is a site which is particularly susceptible to inflammatory accumulation of ^{18}F-FDG, we included a lung tumour xenograft and finally a multi-chemoresistant osteosarcoma [19]. Thus far, there has been no study characterising the pharmacokinetics of ^{18}F-FASu in relation to xCT expression. We therefore compare dynamic ^{18}F-FASu and ^{18}F-FDG uptake characteristics together with parameters from full pharmacokinetic modelling, and relate uptake kinetics to protein expression in the panel of tumour xenografts.

Materials and methods

Animals and tumour xenograft model

Two breast cancers (ER+/PR+ HBCx3 and triple-negative MAS98.12), one osteosarcoma (TPMX) and one lung (A549) cancer xenograft were included in the study. Twelve female nude athymic Foxn1$^{nu/nu}$ mice were bilaterally implanted with tumours under sevoflurane anaesthesia (3%). HBCx3, MAS98.12 and TPMX were implanted as xenograft tissue pieces of ~1 mm^3 obtained from previous passage. A549 was inoculated by subcutaneous injection (s.c.) of ~10^6 cells in a volume of 100 μl. Orthotopic breast cancer xenografts were implanted in the mammary fat pads, whilst ectopic lung and osteosarcoma xenografts were implanted in the flanks. Tumours were then allowed to develop for 3 weeks for A549, 5–6 weeks for MAS98.12, 7–8 weeks for TPMX and 8–10 weeks for HBCx3. Tumour size was measured with callipers and volume was estimated by $\pi/6 \times \text{length} \times \text{width}^2$, where length is the longest tumour diameter and width is that orthogonal to it. Median (range) measured tumour volumes, in units of cubic millimetres, were 93 (55–262) for A549, 477 (127–673) for TPMX, 573 (258–637) for HBCx3 and 1111 (419–1341) for MAS98.12. Mice were kept under sterile conditions, at constant temperature (21.5 ± 0.5 °C) and humidity (55 ± 5%), with 20 air changes/h and a 12-h light cycle. Food and water (supplemented with 17-β-estradiol (4 mg/l) for oestrogen-dependent HBCx3) was provided ad libitum. All experimental procedures involving animals were approved by the National Animal Research Authority and executed in accordance with the guidelines stipulated by the Federation of European Laboratory Animal Science Associations (FELASA).

Radiopharmaceuticals

^{18}F-FDG was provided by GE Healthcare AS, Oslo, Norway.^{18}F-FASu was produced in-house. The tosylate precursor (2*S*)-di-*tert*-butyl-2-((bis-*tert*-butoxycarbonyl)amino)-5-(tosyloxy)octanedioate for radiolabelling was prepared from *N*-boc-L-glutamic acid 1-tert-butyl ester over six steps using methods described elsewhere [9]. Radiolabelling was accomplished by nucleophilic substitution using ^{18}F-KF(crypt-222) in DMSO at 110 °C for 10 min, followed by semi-preparative high-performance liquid chromatography (HPLC (HSF5-C_{18} 5 μm, 250 × 10 mm, 65% CH_3CN-35% H_2O, flow rate 4 mL/min) purification. The subsequent acid hydrolysis (4 N HCl in dioxane) was performed at 90 °C for 10 min, and the product was purified using a tC_{18} cartridge. The final tracer 5-^{18}F-fluoro-L-aminosuberic acid (^{18}F-FASu) was formulated in 0.9% saline and passed through a 0.22-μm filter for further biological studies.

Dynamic PET imaging

Animals were subjected to fasting overnight (~8 h), anaesthetised (1.0 L/min, 1.5% isoflurane in oxygen, Abbott Laboratories, Chicago, IL, USA) and catheterised in the tail vein before being placed prone in groups of three with tumours centred in the gantry of a Siemens microPET Focus 120 pre-clinical scanner (Erlangen, Germany). Scatter and attenuation correction was obtained by 10-min transmission scans using a ^{68}Ge point source. Emission scans were then initiated before intravenous (i.v.) injection of 5–10 MBq of either ^{18}F-FASu or ^{18}F-FDG, and list-mode data were collected for 60 min. Mice were scanned in the same order at each imaging session, during which they were kept warm using insulating wrapping gauze and an infrared lamp. Body temperature was monitored by rectal probe in a representative mouse and maintained at ~35 °C.

PET images were reconstructed using a 3D ordered-subset expectation maximisation followed by a maximum a posteriori (OSEM3D-MAP) algorithm with two OSEM iterations, 18 MAP iterations, $\beta = 0.5$, matrix size = 128 × 128 × 95 and voxel size = 0.87 × 0.87 × 0.80 mm^3. Images were reconstructed into a 48-frame dynamic sequence of 24 × 5 s, 6 × 20 s, 4 × 30 s, 2 × 60 s, 2 × 90 s, 10 × 300 s.

Image analysis

All PET image analysis was performed in IDL 8.3 (ITT Visual Information Solutions, Boulder, CO, USA). Full tumour volumes were delineated manually in the axial plane in final frame images. Injected activity for normalisation of data for individual mice was estimated as previously described [20], and ranged from 4.2 to 7.9 MBq (median 5.5 MBq). SUV time–activity curves (TACs) were generated for all, voxels and the median of the non-necrotic fraction (determined by auto-segmentation of CD31-stained tumour sections, see supplementary file) of highest-uptake voxels at 60 min p.i. was used to quantify uptake in tumours. For further quantification of raw data, we define early SUV (SUV_E) as mean uptake over 0–2 min p.i. and late SUV (SUV_L) as that of the final 5-min frame.

Individual image-derived arterial input functions (AIFs) were obtained by automatic segmentation of images averaged over 0–30 s p.i. A volume containing free tracer was extracted by seeded region growing in the left ventricle. The median TAC over this volume was fitted to a tri-exponential function by Levenberg-Marquardt least squares minimisation, with the resulting fit representing the AIF.

Five mice were excluded from the ^{18}F-FDG data due to faulty injections or experimental failure, including all mice implanted with MAS98.12. All tumour TACs were shifted to a common temporal origin using the time delay of the corresponding AIF peak, and interpolated to a uniform time axis with range of 0–50 min and resolution of 5 s.

Pharmacokinetic modelling

Pharmacokinetic models were fitted to ^{18}F-FASu and ^{18}F-FDG median tumour TACs. For ^{18}F-FDG TACs, a two-tissue compartment model with irreversible binding (rate constants K_1–k_3, $k_4 = 0$) and fractional blood volume, v_B, was applied by convention, as described elsewhere [21]. For ^{18}F-FASu TACs, a (i) simple one-compartment model and (ii) irreversible and (iii) reversible two-compartment models, all including v_B, were applied and suitability assessed using the Akaike information criterion (AIC) [22] (see supplementary file). The two-tissue compartment model with reversible binding was found to be preferable for 14 out of 20 tumours, the remaining 6 being roughly equally well described by both two-tissue compartment models. All ^{18}F-FASu TACs were therefore fit with the full two-tissue compartment model with parameters K_1–k_4 and v_B.

Immunohistochemistry and Western blotting

After completion of imaging, tumours were excised and divided in two. Half was snap-frozen in liquid nitrogen and stored at −80 °C, for frozen sectioning and protein extraction. The other half was formalin-fixed and embedded in paraffin before being sliced in 5-μm sections for immunohistochemical analysis. A549 tumours were small, and the entire excised tumours were therefore fixed in formalin. A new proxy set of A549 tumours were implanted in mice, allowed to develop for 3 weeks, and harvested for comparison with PET data at the group level.

Immunohistochemistry was performed on all tumours with primary polyclonal rabbit antibodies against GLUT1 (1:200, ab15309, Abcam, UK) and CD31 (1:50, ab28364, Abcam,

UK). GLUT1 staining was performed for assessment of membrane glucose transporter levels for relation to ^{18}F-FDG uptake, while CD31 staining was performed to evaluate tumour vascularity. Levels of xCT were quantified by western blotting (1:1000, NB300-318, Novus Biologicals, USA). See supplementary file for detailed protocols and scoring. For correlation of PET data with xCT expression, A549 PET data were averaged to give single group level data points for correlation with mean A549 xCT expression from proxy tumours.

Statistics

The squared Pearson correlation coefficient, r^2, was used to evaluate goodness of fit of pharmacokinetic modelling to raw data. Pearson's correlation coefficient, r, was used to evaluate correlations between PET data. Wilcoxon rank-sum tests were used to test for differences in data between tracers. Kruskal–Wallis tests by ranks with post hoc Dunn tests were used to assess differences in data between tumour groups.

Results

Comparison of dynamic ^{18}F-FASu and ^{18}F-FDG PET across xenograft groups

Dynamic PET scans were successfully obtained for eleven and seven mice injected with ^{18}F-FASu and ^{18}F-FDG, respectively. A total of 34 tumours were delineated; 20 in the ^{18}F-FASu-images (A549: 6, TPMX: 4, HBCx3: 6, MAS98.12: 4) and 14 in the ^{18}F-FDG-images (A549: 6, TPMX: 2, HBCx3: 6), of which a subset of 12 tumours were imaged with both tracers. There was good agreement between tumour volumes delineated in both ^{18}F-FASu and ^{18}F-FDG images ($r = 0.98$, $p < 0.001$) and between all delineated and measured tumour volumes ($r = 0.82$ for ^{18}F-FASu and $r = 0.82$ for ^{18}F-FDG, both $p < 0.001$).

Figure 1 displays early and late PET images of comparative coronal sections of ^{18}F-FASu and ^{18}F-FDG uptake in a representative mouse implanted with TPMX. Heterogeneous features in tumour uptake are recognisable between tracers; however, dynamic distribution differed: early uptake was higher for ^{18}F-FASu, but this was not retained, giving higher late uptake of ^{18}F-FDG. Still, ^{18}F-FASu had a favourable biodistribution with very low background; in particular myocardial uptake was much less pronounced than that of ^{18}F-FDG.

Figure 2 shows mean ^{18}F-FASu (A) and ^{18}F-FDG (B) TACs for the different xenograft groups. The uptake profile of ^{18}F-FASu was characterised by swift influx, giving an initial peak within the first 15 min, followed by a marked clearance phase for MAS98.12 and TPMX. Conversely, A549 and HBCx3 showed a rapid initial uptake followed by a plateau phase or slow clearance, respectively. ^{18}F-FDG uptake was less rapid initially, but generally showed continuous accumulation over the 60-min PET acquisition for most tumours. The early tracer uptake was significantly higher for ^{18}F-FASu than for ^{18}F-FDG across all xenograft groups, as reflected by mean

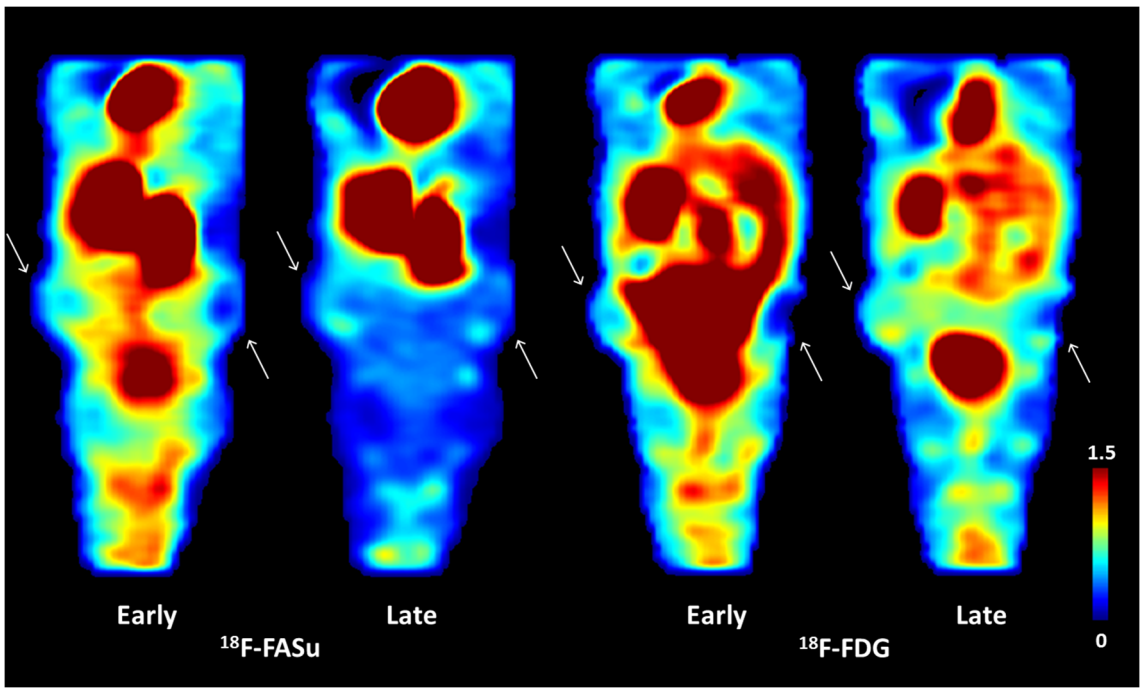

Fig. 1 Coronal PET images of a Foxn1$^{nu/nu}$ mouse with TPMX tumour xenografts examined with ^{18}F-FASu (**a**) and ^{18}F-FDG (**b**). For each tracer, early (3–8 min p.i.) and late (50 min p.i.) acquisitions are shown to the left and right, respectively. Tumours are indicated by arrows.

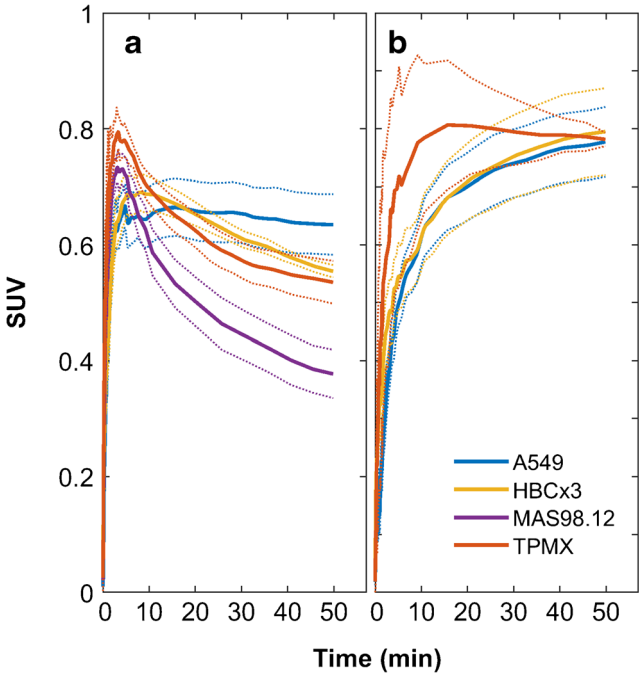

Fig. 2 Dynamic PET TACs for ^{18}F-FASu (**a**) and ^{18}F-FDG (**b**) for the four different xenograft groups, with solid and dotted lines respectively representing the mean and mean ± SEM per group. A549 ($n_{FASu} = 6$, $n_{FDG} = 6$), HBCx3 ($n_{FASu} = 6$, $n_{FDG} = 6$), MAS98.12 ($n_{FASu} = 4$, $n_{FDG} = 0$) and TPMX ($n_{FASu} = 4$, $n_{FDG} = 2$)

(±SEM) SUV_E of 0.44 ± 0.03 for ^{18}F-FASu and 0.24 ± 0.04 for ^{18}F-FDG ($p = 0.007$). However, ^{18}F-FDG had significantly higher uptake than ^{18}F-FASu for time points greater than 20 min p.i., with mean SUV_L of 0.54 ± 0.03 for ^{18}F-FASu and 0.79 ± 0.04 for ^{18}F-FDG ($p < 0.001$).

Reversible and irreversible pharmacokinetic models using individual AIFs were fitted to ^{18}F-FASu and ^{18}F-FDG TACs, respectively, yielding parameters K_1–k_4 and v_B. Agreement between raw and fitted data was overall very good, with median (range) r^2 of 0.97 (0.87–0.99) for ^{18}F-FASu and 0.99 (0.96–1.00) for ^{18}F-FDG. Pharmacokinetic parameters (K_1–k_4 and v_B) and SUV_E and SUV_L obtained for all tumours are tabulated in Table 1. When comparing data over the subset of tumours imaged with both tracers, K_1 was significantly higher for ^{18}F-FASu than for ^{18}F-FDG ($p < 0.001$).

Correlations in PET and immunostaining data

Figure 3a-c summarises results from xCT, GLUT1 and CD31 immunostaining. xCT was expressed in all tumours. Relative levels of xCT were significantly higher for MAS98.12 than for all other tumour groups ($p = 0.042$ against TPMX, $p < 0.002$ against A549 and HBCx3). GLUT1 scores varied considerably across xenografts, with limited extent and intensity for A549 and HBCx3 in contrast to extensive and intense staining for MAS98.12 and TPMX. Median (range) necrotic fractions were 0 (0) for A549, 0.29 (0.20–0.55) for HBCx3, 0.03 (0.02–0.08) for MAS98.12 and 0.36 (0.15–0.40) for TPMX.

Intra-tracer K_1 and SUV_E were strongly correlated, with $r = 0.73$ and $r = 0.82$ (both $p < 0.001$) for ^{18}F-FASu and ^{18}F-FDG, respectively (see supplementary file). SUV_E was also strongly correlated with v_B within tracers ($r = 0.78$ for ^{18}F-FASu and $r = 0.74$ for ^{18}F-FDG, both $p < 0.001$). Although ^{18}F-FDG PET data were missing for MAS98.12, inter-tracer

Table 1 Pharmacokinetic parameters and early and late standardised uptake values (SUV_E and SUV_L, respectively) derived from dynamic ^{18}F-FASu and ^{18}F-FDG PET TACs per xenograft line

		K_1	k_2	k_3	k_4	v_B	SUV_E	SUV_L
^{18}F-FASu	A549	0.077 (0.071–0.089)	0.235 (0.152–0.258)	0.044 (0.039–0.050)	0.008 (0.008–0.012)	0.007 (0.000–0.029)	0.38 (0.23–0.46)	0.60 (0.51–0.84)
	HBCx3	0.074 (0.063–0.096)	0.181 (0.138–0.215)	0.015 (0.008–0.038)	0.011 (0.000–0.024)	0.041 (0.000–0.054)	0.41 (0.21–0.56)	0.56 (0.51–0.59)
	MAS9812	0.125 (0.091–0.155)	0.347 (0.290–0.415)	0.011 (0.008–0.015)	0.003 (0.000–0.013)	0.028 (0.018–0.060)	0.49 (0.43–0.55)	0.35 (0.32–0.50)
	TPMX	0.129 (0.097–0.162)	0.306 (0.241–0.364)	0.023 (0.016–0.028)	0.000 (0.000–0.004)	0.035 (0.002–0.066)	0.57 (0.39–0.72)	0.52 (0.46–0.63)
^{18}F-FDG	A549	0.042 (0.028–0.051)	0.101 (0.051–0.202)	0.009 (0.002–0.016)	NA	0.001 (0.000–0.012)	0.18 (0.01–0.22)	0.85 (0.56–0.90)
	HBCx3	0.051 (0.042–0.085)	0.193 (0.132–0.339)	0.019 (0.017–0.041)	NA	0.036 (0.001–0.048)	0.28 (0.11–0.50)	0.80 (0.55–1.08)
	TPMX	0.108 (0.062–0.154)	0.270 (0.181–0.360)	0.014 (0.010–0.018)	NA	0.011 (0.000–0.022)	0.34 (0.16–0.53)	0.78 (0.77–0.79)

Median (range) values are given

NA not applicable

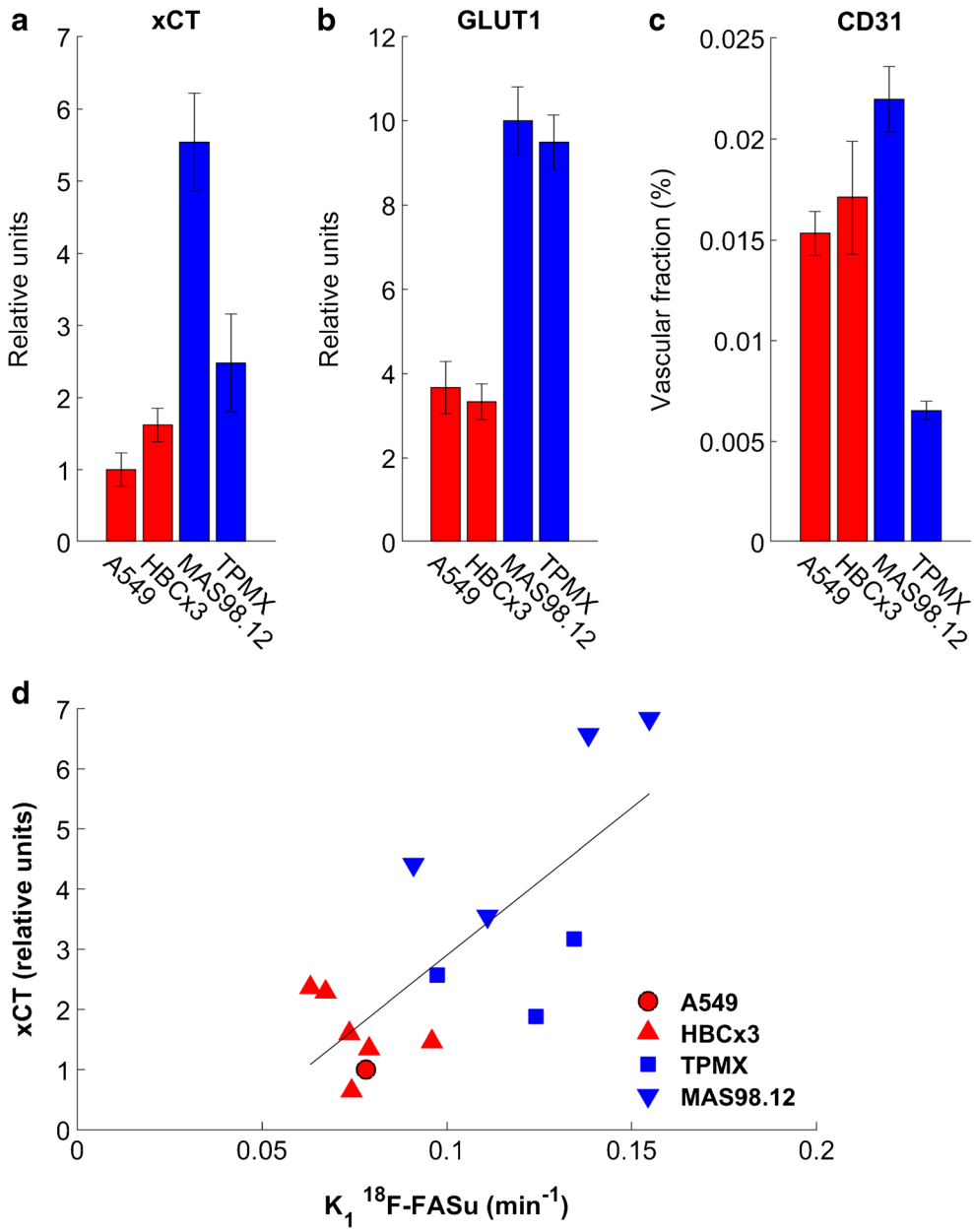

Fig. 3 Immunostaining data against xCT, GLUT1 and CD31. All data are presented as the mean with SEM error bars. (**a**) Relative levels (background-corrected signal normalised to mean A549 signal) of xCT per tumour group. Sample sizes were as follows: A549: $n = 8$, TPMX: $n = 10$, HBCx3: $n = 12$; MAS98.12: $n = 17$. (**b**) GLUT1 scores. (**c**) Vascular fraction as percentage CD31-stained area per non-necrotic tumour area. Sample sizes for GLUT1 and CD31 were $n = 6$ for A549 and HBCx3, and $n = 4$ for MAS98.12 and TPMX. (**d**) Relationship between tracer influx rate and transporter expression for ^{18}F-FASu K_1 and xCT ($p = 0.024$). The A549 data point represents the mean of K_1 for this group ($n = 6$), plotted against mean normalised xCT from proxy tumours. Tumours classified as type α are shown in red, and type β in blue

K_1($r = 0.85$), v_B ($r = 0.85$) and SUV_E ($r = 0.80$) from ^{18}F-FASu and ^{18}F-FDG TACs were strongly correlated, all with $p < 0.001$, and there was a significant inverse correlation between tracers in k_3 ($r = -0.59$, $p = 0.042$).

Relative xCT levels were found to correlate positively with K_1 ($r = 0.74$, $p = 0.001$) and k_2 ($r = 0.78$, $p < 0.001$) and inversely with SUV_L ($r = -0.61$, $p = 0.019$) from ^{18}F-FASu PET. GLUT1 was significantly positively correlated with K_1 from both ^{18}F-FDG-scans ($r = 0.70$, $p = 0.004$) and ^{18}F-FASu-scans ($r = 0.61$, $p = 0.004$). Additionally, expression of xCT and GLUT1 were found to correlate significantly ($r = 0.62$, $p = 0.016$). Vascular fractions from CD31 were not significantly correlated with any PET data.

Classification of two different ^{18}F-FASu uptake profiles

On inspection of the ^{18}F-FASu TACs for the four different xenograft lines shown in Fig. 2a, one may categorise them into two main profiles: types α (A549 and HBCx3) and β (MAS98.12 and TPMX). In the pharmacokinetic modelling of ^{18}F-FASu TACs, we found that the majority of tumours (14/20) had a more or less pronounced preference for the reversible model. The type β tumours were largely (6 of 8) indifferent to the choice of model and had lower k_4 compared with the type α tumours ($p = 0.004$). K_1 and k_2, as well as SUV_E, were also significantly higher for the type β tumours ($p < 0.01$).

Type α and β tumours moreover differed in protein expression, with significantly higher xCT and GLUT1 expression (both $p < 0.001$) for type β. Figure 3d shows xCT expression levels plotted against K_1 from ^{18}F-FASu PET.

Discussion

We compared dynamic ^{18}F-FASu and ^{18}F-FDG PET uptake patterns together with protein expression levels in a panel of four tumour xenograft lines. Most noteworthy, the influx rate of ^{18}F-FASu was significantly positively associated with xCT expression levels. In contrast to data reported by Yang et al. [10], we found a significant inverse relationship between xCT expression and SUV_L. Overall, uptake of ^{18}F-FASu and ^{18}F-FDG was on the same scale, but their dynamic uptake profiles differed, which was demonstrated by significant differences in SUVs at different time points p.i. and in pharmacokinetic modelling parameters.

Comparing ^{18}F-FASu and ^{18}F-FDG PET TACs for this panel of xenografts, tumours accumulate less ^{18}F-FASu, with mean SUV_L being nearly 50% higher for ^{18}F-FDG. Early uptake, however, is markedly higher for ^{18}F-FASu, with both SUV_E and K_1 about 60% lower for ^{18}F-FDG, which may imply differences in tracer diffusion across the blood vessel walls in the early tissue distribution phase. Although the tracers are of similar molecular weight (182 for ^{18}F-FASu and 181 g/mol for ^{18}F-FDG), this could point to a greater steric hindrance of ^{18}F-FDG, but also to differences in transporter affinity (see below). In any case, v_B was of comparable magnitude for the two tracers studied, indicating that the pharmacokinetic estimates of intravascular blood volume fraction (which should be the same regardless of tracer used) were consistent.

In the current work, we found that expression of xCT was significantly correlated with K_1 for ^{18}F-FASu. Correspondingly, GLUT1 expression was significantly correlated with K_1 for ^{18}F-FDG, in agreement with previous studies [17, 23, 24]. This could indicate that membrane transport is a rate-limiting factor for cellular uptake, making K_1 dependent not only on perfusion and vascular permeability, but also on receptor availability and ligand binding characteristics. The significantly lower K_1 for ^{18}F-FDG, therefore, may also be in part the result of lower affinity of ^{18}F-FDG for GLUT1 receptors compared with that of ^{18}F-FASu for xCT. We also found that xCT and GLUT1 expression levels in tumours were significantly correlated, which accords with the recent finding that xCT expression, like GLUT1 [25], is negatively regulated by glucose availability [26]. The observed strong correlation of K_1s from ^{18}F-FASu and ^{18}F-FDG PET TACs may as such reflect not only the same vascular anatomy, but also in part this co-behaviour in regulation of transporters. CD31 data were not found to correlate with estimated blood volume fractions from either ^{18}F-FASu- or ^{18}F-FDG PET data. Given the high consistency in v_Bs derived from ^{18}F-FASu- and ^{18}F-FDG-TACs, this is likely not due to inherent noise in the parameter, but rather that indiscriminate staining of endothelium may not be fully representative of functional vessels in the tumour xenografts.

Regarding uptake levels in the xenograft lines, our findings differ from those presented by Webster et al. [9] and Yang et al. [10]. Webster et al. reported a mean SUV at 60 min p.i. of 2.5 for ^{18}F-FASu in SKOV-3 ovarian cancer xenografts, more than fivefold higher than mean SUV for ^{18}F-FDG [9]. Moreover, the dynamic ^{18}F-FASu PET TACs for EL4 lymphoma xenografts showed strictly accumulative uptake over the first hour, with mean tumour tracer concentration of just below 1.5% of the injected dose (%ID)/cm^3 from the first frame at roughly 2 min p.i., to a level just above 6% ID/cm^3 at 60 min p.i. Biodistribution tumour-to-blood ratios at 50 min p.i. were around 12 for both xenograft lines. Translating our results to %ID/cm^3, we find comparable early uptake over the first 2 min p.i., with group means ranging from 1.4 %ID/cm^3 for A549 to 2.1 %ID/cm^3 for TPMX. Late uptake however, is considerably lower, at most 2.4 %ID/cm^3 for A549 at 60 min p.i. Mean tumour-to-blood ratios were about 0.9 for the two breast cancer lines (MAS98.12 and HBCx3) and 2.0 for lung cancer (A549). Even when considering SUV_{max}, tumour-to-blood ratios were no greater than 3.0 ± 0.4 (A549). Considering uptake of ^{18}F-FASu in relation to xCT expression, Yang et al. [10] compared ^{18}F-FASu uptake in breast cancer models of different histological subtypes, finding significantly elevated expression of xCT and correspondingly higher uptake of ^{18}F-FASu at 120 min p.i. for triple-negative MDA-MB-231 tumours (1.38 ± 0.27 %ID/g) compared with ER+/PR+ tumour lines MCF-7 and ZR-75-1 (1.01 ± 0.20 and 0.75 ± 0.14, respectively). These values are comparable to late uptake in our xenografts. Recent work by Čolović et al. also shows PET tumour-to-blood ratios for MDA-MB-231 tumours increasing to not much greater than 1 at 55 min p.i. [27], in agreement with our MAS98.12 data. Comparing triple-negative MAS98.12 with ER+/PR+ HBCx3, we too found higher levels of xCT in the triple-negative subtype, corresponding to significantly higher ($p = 0.010$) initial uptake of ^{18}F-FASu. However, this did not result in high uptake at late time points p.i., with SUV_L for MAS98.12 being significantly lower than that for HBCx3. This indicates that higher xCT-mediated transport does not necessarily lead to increased retention of ^{18}F-FASu.

Considering the two different uptake profiles identified, one may discuss the possible underlying biochemical processes. The k_2 tracer efflux rate exhibited a slightly stronger correlation with xCT than did K_1. This could indicate that ^{18}F-FASu may exit cells through system X_c^- in exchange for endogenous cystine, analogously with glutamate. This may well be, as ^{18}F-FASu has structural characteristics of both cystine

and glutamate. The high efflux seen in type β tumours could thus be simply the result of high xCT activity. On the other hand, one may consider that the type α and β TAC profiles reflect two disparate redox strategies for the different tumour xenografts. Type α could appear to focus on intracellular reduction by utilisation of more modest levels of imported cystine for glutathione synthesis, reflected by a greater retention of ^{18}F-FASu. Conversely, type β tumours may have a greater demand for extracellular antioxidants, and prioritise export of intracellularly reduced cysteine, resulting in high washout of ^{18}F-FASu. Banjac et al. indeed found that the protective effect of system X_c^- against oxidative stress is mediated mainly by maintenance of exceedingly high extracellular levels of cysteine through the cystine/cysteine redox cycle, rather than increased intracellular levels of cysteine and GSH [28, 29].

Dynamic ^{18}F-FASu PET (or combination of an early and a late scan) could be useful for assessment of cysteine/glutamate antiporter expression and thus of oxidative stress. Low uptake at 60 min p.i. is not necessarily indicative of a low-grade tumour with low xCT expression, but may rather reflect advanced disease with a highly oxidative extracellular milieu. New PET technology capable of fast whole-body dynamic imaging in more or less the same length of time as a conventional static late scan is becoming increasingly available [30]. Dynamic ^{18}F-FASu PET could also be informative in predicting response to therapy. Chemotherapeutics generate high levels of reactive oxygen species as part of their mechanism of action [30], and the TAC profile displayed by TPMX and MAS98.12 (type β) may indicate lowered sensitivity to the oxidative stress component of chemotherapies. TPMX is reportedly highly resistant to a range of chemotherapeutics [19], and it may well be that the efficient use of the cystine/cysteine redox cycle plays a part in this.

Conclusion

Dynamic imaging and pharmacokinetic analysis revealed that early ^{18}F-FASu uptake rate (K_1) reflected xCT expression, showing that dynamic ^{18}F-FASu PET with pharmacokinetic modelling may shed light on oxidative stress and different redox strategies in tumours. ^{18}F-FASu PET could thus be valuable for staging and assessment of therapy response.

Funding This study was funded by the University of Oslo (convergence grants) and the Norwegian Cancer Society (grant 6871141-2015).

Compliance with ethical standards

Conflict of interest The authors declare that they have no conflict of interest.

Ethical approval All applicable international, national, and/or institutional guidelines for the care and use of animals were followed.

References

1. Inoue T, Kim EE, Komaki R, Wong FCL, Bassa P, Wong W-H, et al. Detecting recurrent or residual lung cancer with FDG-PET. J Nucl Med. 1995;36:788–93.
2. Hamada K, Tomita Y, Inoue A, Fujimoto T, Hashimoto N, Myoui A, et al. Evaluation of chemotherapy response in osteosarcoma with FDG-PET. Ann Nucl Med. 2009;23:89–95. https://doi.org/10.1007/s12149-008-0213-5.
3. McDermott GM, Welch A, Staff RT, Gilbert FJ, Schweiger L, Semple SI, et al. Monitoring primary breast cancer throughout chemotherapy using FDG-PET. Breast Cancer Res Treat. 2007;102:75–84.
4. Gulyas B, Halldin C. New PET radiopharmaceuticals beyond FDG for brain tumor imaging. Q J Nucl Med Mol Imaging. 2012;56:173–90.
5. Salminen E, Hogg A, Binns D, Frydenberg M, Hicks R. Investigations with FDG-PET scanning in prostate Cancer show limited value for clinical practice. Acta Oncol. 2002;41:425–9. https://doi.org/10.1080/028418602320405005.
6. Rosenbaum SJ, Lind T, Antoch G, Bockisch A. False-positive FDG PET uptake−the role of PET/CT. Eur Radiol. 2006;16:1054–65. https://doi.org/10.1007/s00330-005-0088-y.
7. Baek S, Choi C-M, Ahn SH, Lee JW, Gong G, Ryu J-S, et al. Exploratory clinical trial of (4S)-4-(3-[18F]fluoropropyl)-l-glutamate for imaging xC− transporter using positron emission tomography in patients with non–small cell lung or breast Cancer. Clin Cancer Res. 2012;18:5427–37. https://doi.org/10.1158/1078-0432.ccr-12-0214.
8. Baek S, Mueller A, Lim Y-S, Lee HC, Lee Y-J, Gong G, et al. (4S)-4-(3-18F-fluoropropyl)-l-glutamate for imaging of xC transporter activity in hepatocellular carcinoma using PET: preclinical and exploratory clinical studies. J Nucl Med. 2013;54:117–23.
9. Webster JM, Morton CA, Johnson BF, Yang H, Rishel MJ, Lee BD, et al. Functional imaging of oxidative stress with a novel PET imaging agent, 18F-5-fluoro-L-aminosuberic acid. J Nucl Med. 2014;55:657–64.
10. Yang H, Miao Q, Jenni S, Čolović M, Johnson B, Rishel M, et al. [18F] 5-fluoro aminosuberic acid (FASu) for oxidative stress imaging in breast cancer. J Nucl Med. 2015;56:1176.
11. Sosa V, Moliné T, Somoza R, Paciucci R, Kondoh H, Lleonart ME. Oxidative stress and cancer: an overview. Ageing Res Rev. 2013;12:376–90. https://doi.org/10.1016/j.arr.2012.10.004.
12. Landriscina M, Maddalena F, Laudiero G, Esposito F. Adaptation to oxidative stress, chemoresistance, and cell survival. Antioxid Redox Signal. 2009;11:2701–16. https://doi.org/10.1089/ars.2009.2692.
13. Belotte J, Fletcher NM, Awonuga AO, Alexis M, Abu-Soud HM, Saed MG, et al. The role of oxidative stress in the development of cisplatin resistance in epithelial ovarian cancer. Reprod Sci. 2014;21:503–8. https://doi.org/10.1177/1933719113503403.
14. Sato H, Tamba M, Ishii T, Bannai S. Cloning and expression of a plasma membrane cystine/glutamate exchange transporter composed of two distinct proteins. J Biol Chem. 1999;274:11455–8.
15. Conrad M, Sato H. The oxidative stress-inducible cystine/glutamate antiporter, system x c − : cystine supplier and beyond. Amino Acids. 2012;42:231–46. https://doi.org/10.1007/s00726-011-0867-5.
16. Koeppe RA, Frey KA, Vander Borght TM, Karlamangla A, Jewett DM, Lee LC, et al. Kinetic evaluation of [11C]Dihydrotetrabenazine by dynamic PET: measurement of vesicular monoamine transporter. J Cereb Blood Flow Metab. 1996;16:1288–99. https://doi.org/10.1097/00004647-199611000-00025.
17. Kristian A, Nilsen LB, Røe K, Revheim M-E, Engebråten O, Mælandsmo GM, et al. Dynamic 18 F-FDG PET for assessment of tumor physiology in two breast carcinoma xenografts. Nucl Med Mol Imaging. 2013;47:173–80.

18. Kristian A, Riss P, Qu H, Milde M, Schoultz BW, Engebraaten O, et al. Positron emission tomography and pharmacokinetics of 2-[18F]-fluoroethyl choline for metabolic studies in breast cancer xenografts. Acta Oncol. 2014;53:1086–92. https://doi.org/10.3109/0284186X.2014.934398.
19. Bruheim S, Bruland OS, Breistol K, Maelandsmo GM, Fodstad Ø. Human osteosarcoma xenografts and their sensitivity to chemotherapy. Pathol Oncol Res. 2004;10:133–41. https://doi.org/10.1007/bf03033741.
20. Pitman KE, Rusten E, Kristian A, Malinen E. Variability of dynamic 18F-FDG-PET data in breast cancer xenografts. Acta Oncol. 2015;54:1399–407.
21. Røe K, Aleksandersen TB, Kristian A, Nilsen LB, Seierstad T, Qu H, et al. Preclinical dynamic 18F-FDG PET-tumor characterization and radiotherapy response assessment by kinetic compartment analysis. Acta Oncol. 2010;49:914–21.
22. Turkheimer FE, Hinz R, Cunningham VJ. On the undecidability among kinetic models: from model selection to model averaging. J Cereb Blood Flow Metab. 2003;23:490–8.
23. Bretschi M, Cheng C, Witt H, Dimitrakopoulou-Strauss A, Strauss LG, Semmler W, et al. Cilengitide affects tumor compartment, vascularization and microenvironment in experimental bone metastases as shown by longitudinal 18F-FDG PET and gene expression analysis. J Cancer Res Clin Oncol. 2013;139:573–83. https://doi.org/10.1007/s00432-012-1360-6.
24. S-l S, Deng C, L-f W, J-j L, Wang H, Feng D, et al. 18F-FDG PET/CT-related metabolic parameters and their value in early prediction of chemotherapy response in a VX2 tumor model. Nucl Med Biol. 2009;37:327–33. https://doi.org/10.1016/j.nucmedbio.2009.12.002.
25. Wertheimer E, Sasson S, Cerasi E, Ben-Neriah Y. The ubiquitous glucose transporter GLUT-1 belongs to the glucose-regulated protein family of stress-inducible proteins. Proc Natl Acad Sci U S A. 1991;88:2525–9. https://doi.org/10.1073/pnas.88.6.2525.
26. Koppula P, Zhang Y, Shi J, Li W, Gan B. The glutamate/cystine antiporter SLC7A11/xCT enhances cancer cell dependency on glucose by exporting glutamate. J Biol Chem 2017:jbc. M117. 798405.
27. Čolović M, Rousseau E, Zhang Z, Lau J, Zhang C, Kuo H-T, et al. Synthesis and evaluation of an 18F-labeled boramino acid analog of aminosuberic acid for PET imaging of the antiporter system xC−. Bioorg Med Chem Lett. 2018;28:3579–84.
28. Banjac A, Perisic T, Sato H, Seiler A, Bannai S, Weiss N, et al. The cystine/cysteine cycle: a redox cycle regulating susceptibility versus resistance to cell death. Oncogene. 2007;27:1618. https://doi.org/10.1038/sj.onc.1210796 https://www.nature.com/articles/1210796#supplementary-information.
29. Osborne DR, Acuff S. Whole-body dynamic imaging with continuous bed motion PET/CT. Nucl Med Commun. 2016;37:428–31. https://doi.org/10.1097/MNM.0000000000000455.
30. Conklin KA. Chemotherapy-associated oxidative stress: impact on chemotherapeutic effectiveness. Integr Cancer Ther. 2004;3:294–300. https://doi.org/10.1177/1534735404270335.